RSC
Applied Interfaces

PAPER

Check for updates

Densely atomic Co–Nx moiety-coupled hierarchical-carbon-microspheres for efficient oxygen electrodes in bioadaptable Mg–air batteries†

Yanru Liu,‡[a] Taiqiang Dai,‡[a] Jia Wang,[a] Lirong Zheng [b] and Xiaogang Fu [*c]

The Mg–air battery is one of the promising candidates for the next generation of bioadaptable power sources. However, it suffers from low efficiency cathodes to facilitate the slow oxygen reduction reaction (ORR). Herein, this work reports a strategy to enhance the density of catalytic active sites and further facilitate their accessibility for advanced air electrodes. A prior spray-assisted stepwise pyrolysis strategy is employed to obtain the densely atomic Co–Nx active site-decorated hierarchically carbon microspheres (Co–Nx–HCM), which are further employed as advanced oxygen electrodes for primary Mg–air batteries. The resulting Co–Nx active sites impart electrodes with good bio-adaptability and decent ORR activity under neutral electrolytes. Furthermore, the hierarchical carbon microspheres endow the air electrode with smooth mass transport. In application of an assembled Mg–air flow battery, the SA Co–Nx–HCM electrode delivers a high open-circuit potential of 1.78 V, a high maximum power density of 34.2 mW cm^{-2}, a decent gravimetric energy density of *ca.* 3441 Wh kg$_{Mg}^{-1}$, and a long operating life over 100 h. This work paves a way to explore single atomic catalysts with hierarchically porous morphology as advanced air cathodes for bioadaptable electronic devices.

1. Introduction

The rapid development of bionic electronics has highlighted the requirements for exploring new energy storage systems.[1–3] The magnesium (Mg)–air battery is a promising candidate due to its high theoretical capacity, low cost and high discharge voltage under neutral conditions.[4–7] Also, Mg or Mg alloys have good bioresorbability, and Mg^{2+} ions generated during battery discharge are beneficial to the human body.[8–10] However, one of the significant difficulties hindering the rapid development of Mg–air batteries is the lack of an efficient air cathode to facilitate the oxygen reduction reaction (ORR).[11–14]

Single atomic transition metals and nitrogen co-doped carbon matrix (SA M–Nx–C) have been reported as promising materials for catalyzing the sluggish ORR.[15–21] Recently, metal–organic-frameworks, especially zeolite imidazole frameworks (ZIF-8), have been developed as ideal precursors to prepare SA M–Nx–C catalysts exhibiting remarkably ORR activity.[22–26] Subsequently, various strategies based on ZIF-8, including the coordination effect,[27–31] chemical bonding,[32–34] and spatial confinement,[35–37] have been explored to enhance the density of M–Nx active sites. Despite the great process, it remains challenging to further increase the active site density as the agglomeration/migration of single metal atoms into clusters or nanoparticles during high-temperature treatment leads to a relatively weak catalytic activity.[38–40] Furthermore, the actual catalytic performance of these ZIF-8 developed SA M–Nx–C catalysts becomes limited due to the restricted diffusion of ions and air caused by the non-accessible and blocked structure of the cathodes.[41,42] Therefore, three-dimensional (3D) porous structures in a catalyst for facilitating mass transport and building efficient three-phase interfaces for the ORR in air electrodes are highly desired.[43–45] However, to achieve these 3D porous structures, the routine methods always used silicon-based templates, which inevitably introduce complicated removal treatments and are challenging for scalable production.[46–48] Thus,

[a] *State Key Laboratory of Oral & Maxillofacial Reconstruction and Regeneration, National Clinical Research Center for Oral Diseases, Shaanxi Key Laboratory of Stomatology, Department of Dental Materials, School of Stomatology, The Fourth Military Medical University, Xi'an, ShannXi, 710032, P. R. China*
[b] *Beijing Synchrotron Radiation Facility (BSRF), Institute of High Energy Physics Chinese Academy of Sciences, Beijing 100049, P. R. China*
[c] *State Key Laboratory of Solidification Processing, Atomic Control & Catalysis Engineering Laboratory, School of Materials Science and Engineering, Northwestern Polytechnical University, Xi'an, Shaanxi, 710072, P. R. China. E-mail: xiaogangfu@nwpu.edu.cn*
† Electronic supplementary information (ESI) available. See DOI: https://doi.org/10.1039/d4lf00408f
‡ Yanru Liu and Taiqiang Dai contributed equally to this study.

developing a facile strategy for preparing dense atomically dispersed M–Nx–C catalysts with 3D hierarchical porosity is particularly appealing.

To address these challenges, we report a prior spray-assisted stepwise pyrolysis strategy to prepare densely single atomic Co-Nx active site-incorporated hierarchical-carbon-microspheres (SA Co-Nx–HCM) as competent oxygen electrodes for Mg–air batteries. The main preparation procedures include a prior spray drying of fresh synthesized zeolitic imidazolate frameworks (ZIF-8) to form a 3D hierarchical micro-spheric support followed by a stepwise pyrolysis treatment for stabilizing dense Co–Nx active sites. It is noteworthy that the SA Co–Nx–HCM shows good bio-adaptability and decent oxygen electrocatalytic performances in neutral electrolytes. The air electrode built with the SA Co–Nx–HCM catalyst possesses a 3D porous structure, facilitating the ion/air diffusion and imparting the assembled Mg–air battery with good activity and stability performance.

2. Experimental

2.1. Synthetic procedures

The ZIF-8 crystals were synthesized according to the previous literature.[46] Then, 10.0 g of the pristine ZIF-8 nanoparticles were dispersed in deionized water and then spray dried at 200 °C to construct ZIF-8-based hierarchical porous microspheres.[49] After heat-treating at 700 °C for 1 h in Ar, the hierarchical-carbon-microsphere (HCM) support was obtained. Then, 100.0 g of HCM was dispersed in 30.0 mL of n-hexane while sonicating for 30 min. Next, $Co(NO_3)_2$ aqueous solution (300 mg ml^{-1}, 30 μL) was added to the mixed solution and sonicated for 3 h. Then, the obtained precipitate was washed with deionized water 3 times and dried. Finally, the resulting materials were heated at 900 °C in Ar for 2 h to yield SA Co–Nx–HCM. For comparison, pristine ZIF-8 nanocrystals were directly used without spray drying and were treated in the same way as SA Co–Nx–HCM to fabricate SA Co–Nx–C. The sample prepared by directly pyrolyzing ZIF-8 and $Co(NO_3)_2$ was denoted as Co–N–C.

2.2. Material characterization

All the materials' elemental compositions were detected using X-ray photoelectron spectroscopy (XPS). The microstructures and morphology were obtained by using a high-resolution transmission electron microscopy instrument (JEOL 2010F microscope). Raman spectra were acquired using a Bruker Senterra Raman instrument. The crystalline phase was identified by powder X-ray diffraction (XRD) (Bruker D8, Cu Kα radiation). A Micromeritics ASAP 3020 instrument was used to analyze the Brunauer–Emmett–Teller (BET) surface area and pore size distribution data. The Co content was measured by inductively coupled plasma optical emission spectrometry (ICP-OES, Thermo Fisher Scientific). The Co K-edge XAS measurements were conducted at the beamline 1W1B of the Beijing Synchrotron Radiation Facility (BSRF, Beijing, China). The Athena program was used to process data.

2.3. Evaluation of cytocompatibility

To investigate the biocompatibility of SA Co–Nx–HCM, the CCK8 test and live/dead staining were performed.[50] For the cell counting kit-8 (CCK8) test, third passage bone mesenchymal stem cells (BMSCs) were seeded in 96 well plates (2000 cells per well, 100 μl) and cultured for 24 hours. The culture medium was changed with fresh α-MEM medium containing 1.5 μg ml^{-1} of SA Co–Nx–HCM. At 1, 2, 3, 5, and 7 days, 10 μL CCK8 (Plant Chem Med, China) was added to the well, and cells were incubated for another 2 hours. An ELISA reader measured the absorbance at 450 nm.

To assess the viability of cells cultured with SA Co–Nx–HCM, live/dead assay was conducted. Briefly, BMSCs were cultured in confocal dishes for 24 hours, and the culture medium was switched to fresh medium with 1.5 μg ml^{-1} of SA Co–Nx–HCM. After 7 days, the cells were incubated with Calcein-AM/Propidium Iodide (AM/PI) (Beyotime Biotechnology, China) staining solution at 37 °C for 30 minutes in the dark according to the manufacturer's instructions. Finally, the cells were observed and photographed under a laser confocal microscope (Nikon A1+, Japan).

3. Results and discussion

As shown in Fig. 1, we developed a spray-assisted stepwise pyrolysis approach to obtain densely single atomic Co–Nx active site-decorated hierarchically carbon microspheres. First, pristine ZIF-8 nanocrystals were subjected to a spray-drying treatment to form porous microspheres with diameter sizes of ca. 0.5 μm

Fig. 1 Synthetic scheme for the preparation of SA Co–Nx–HCM catalyst.

(Fig. S1a†). Next, heat treatment at 700 °C was applied to maintain the integrity of this spheric morphology (Fig. S1b†) and prevent it from crushing during the post-treatment. Moreover, abundant nitrogen-doped microporous defects were generated after pyrolysis, as evidenced by BET and XPS data. The t-plot analysis indicates that the micropore surface area (390 m^2 g^{-1}) accounts for 81.3% of the overall surface area (480 m^2 g^{-1}, Table S1†). Also, the XPS results show the overall N content is ca. 5.41 at%. Such ample micropores with N dopants are ideal carbon matrices to fabricate atomic active sites effectively.[51–53] Finally, the nitrogen-doped carbon spheres were subjected to absorbing Co^{2+} ions and undergoing a second pyrolysis and post-treatment, obtaining SA Co–Nx–HCM. Obviously, the SA Co–Nx–HCM catalyst maintains the spherical and porous morphology (Fig. 2a and b). The generated pore voids between neighbouring HCM and within HCM can be observed, which are supposed to promote mass transport in the air cathode. In addition, obvious disordered and amorphous structures were detected in the carbon matrix (Fig. S2†), which are supposed to benefit ORR catalysis.[54] The reference sample

SA Co–Nx–C (Fig. S1c†) was prepared without spray-drying, and Co–N–C (Fig. S1d†) was synthesized by directly pyrolyzing ZIF-8 and cobalt salt. Apparently, all SA Co–Nx–HCM, SA Co–Nx–C and Co–N–C show similar adsorption hysteresis loops at high pressure (Fig. 2c), while the SA Co–Nx–HCM (894 m^2 g^{-1}) has a superior surface area compared to SA Co–Nx–C (712 m^2 g^{-1}) and Co–N–C (682 m^2 g^{-1}). The enhanced surface area of SA Co–Nx–HCM is ascribed to the voids between single ZIF-8-derived carbon crystals and the porosity within the assembled microspheres, as its external surface area (317 m^2 g^{-1}) is higher than that of SA Co–Nx–C (213 m^2 g^{-1}) and Co–N–C (197 m^2 g^{-1}, Table S1†). Also, these three samples show significant differences in pore size distribution (Fig. 2d). The SA Co–Nx–C and Co–N–C catalysts prepared without the spray-drying process show similar and narrow pore size distribution, and a large number of pore sizes centred at ca. 4 nm. As for the spray-drying processed SA Co–Nx–HCM catalyst, ample hierarchical pores ranging from 5–120 nm were detected. Such abundant and hierarchical meso/macropores could be employed as effective channels to facilitate reactants and products toward
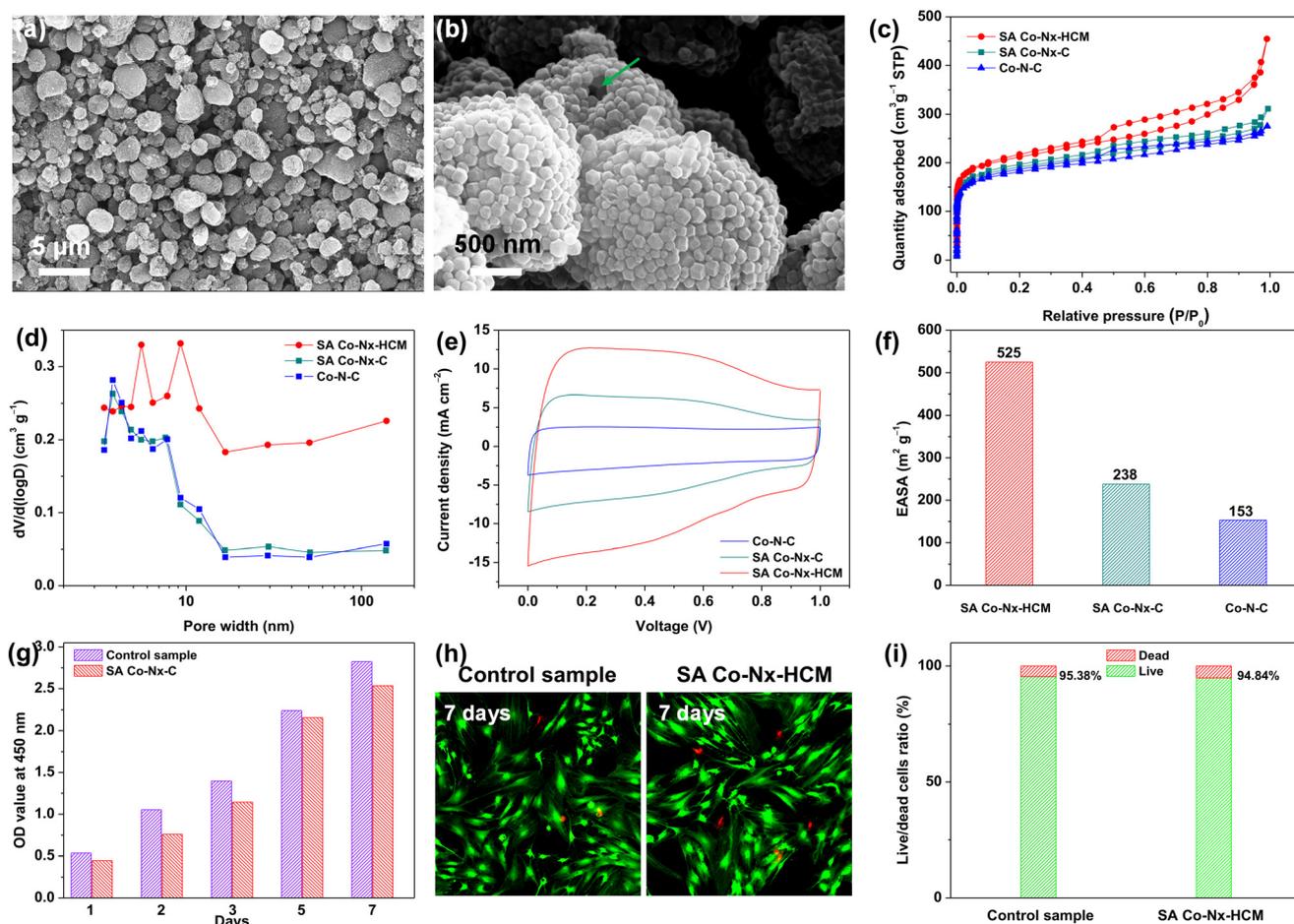

Fig. 2 (a) and (b) SEM images of SA Co–Nx–MPCS. (c) N$_2$ sorption isotherms, (d) the pore size distribution, (e) ECSAs determined in the PBH electrolyte, and (f) comparation of ECSAs for the prepared catalysts. In vitro cytocompatibility analysis of BMSCs cocultured with 1.5 μg ml^{-1} SA Co–Nx–HCM. (g) CCK8 test for BMSCs cocultured with SA Co–Nx–HCM. (h) Representative images of live/dead staining. (i) Live/dead cell ratio of BMSCs for 7 days.

and away from Co–Nx active moieties and improve catalytic performance. However, some portions of the BET surface area cannot be effectively utilized, as electrolytes cannot reach them. Hence, the electrochemically active surface area (ECSA) was obtained to evaluate electrocatalysts' actual active surface areas during the ORR.[55] As shown in Fig. 2e and f, the ECSA of SA Co–Nx–HCM (525 m^2 g^{-1}) is about 2.2 and 3.4 times higher than those of SA Co–Nx–HCM (238 m^2 g^{-1}) and Co–N–C (153 m^2 g^{-1}), respectively, which is in agreement to the trend observed with the BET surface areas. The superior ECSA is related to a high BET surface area and abundant porosity, suggesting that SA Co–Nx–HCM can provide good active site accessibility, smooth mass transport, and therefore better catalytic behaviours. To assess the tissue adaptability of the SA Co–Nx–HCM oxygen electrode, CCK8 tests were applied to evaluate the cytocompatibility in this study. As shown in Fig. 2g, SA Co–Nx–HCM exhibited low cytotoxicity, as the absorbance value at 450

nm significantly decreased when compared with the control sample. In addition, almost no or only a few dead cells were observed in control groups and groups with SA Co–Nx–HCM after 7 days (Fig. 2h and i), suggesting its good cell compatibility. These results guarantee its application potential in oxygen electrodes for bio-adaptable Mg–air batteries.

This spray-assisted stepwise pyrolysis approach is feasible for fabricating dense Co–Nx active sites. The high-angle annular dark-field scanning transmission electron microscopy (HAADF-STEM) images indicate that no observable Co-based aggregates are presented in SA Co–Nx–HCM (Fig. 3a). Also, the elemental mapping reveals that the C, N and Co elements are uniformly distributed. Further, the atomic resolution HAADF-STEM image indicates that Co atoms are atomically dispersed on the carbon spheres (Fig. 3b). These results are in accord with the XRD results, as, except for the broad peak assigned to the (002) facet of graphitic carbon, there is no other diffraction peak of
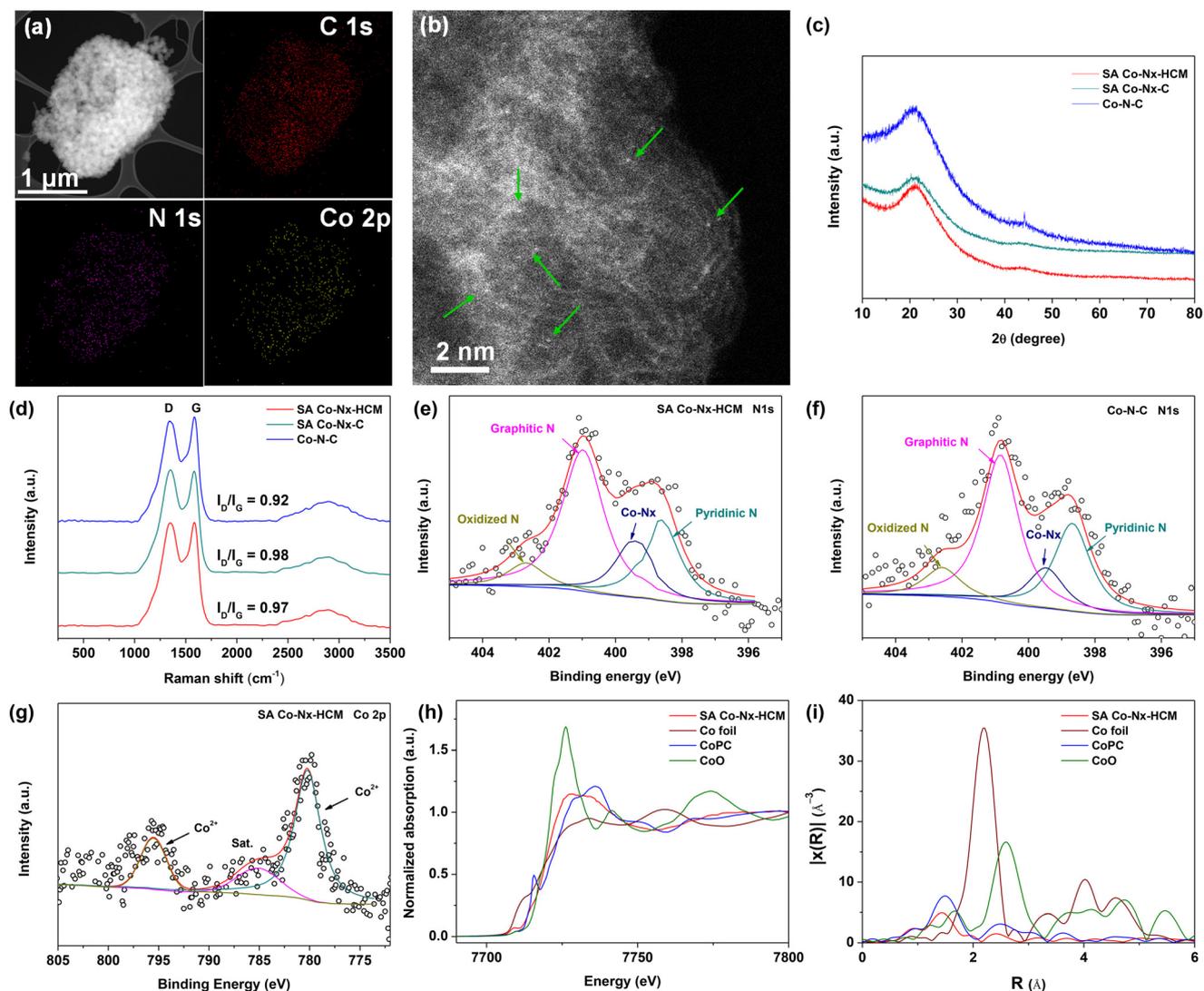

Fig. 3 (a) STEM image and (b) the corresponding elemental mapping of SA Co–Nx–HCM. (c) XRD and (d) Raman patterns of the prepared catalysts. XPS N 1s of (e) SA Co–Nx–HCM and (f) Co–N–C. (g) XPS Co 2p of SA Co–Nx–HCM. (h) Fe K-edge XANES and (i) Fourier transforms of EXAFS spectra of prepared catalysts and references.

© 2025 The Author(s). Published by the Royal Society of Chemistry

RSC Appl. Interfaces, 2025, 2, 696–703 | **699**

crystalline Co species shown in SA Co–Nx–HCM and SA Co–Nx–C (Fig. 3c), confirming the non-formation of cobalt crystals. By contrast, the Co–N–C catalyst prepared by directly pyrolyzing ZIF-8 and $Co(NO_3)_2$ precursor contains a small amount of CoO metallic particles, as demonstrated by the emerged peak at 45° (Fig. 3c) and the TEM analysis (Fig. S3†). The Raman spectra indicate that the I_D/I_G ratio values in SA Co–Nx–HCM (0.97) and SA Co–Nx–HCM (0.98) are higher than that in Co–N–C (0.92), suggesting that Co–N–C has a relatively higher graphitic structure (Fig. 3d). This is probably because trace Co metallic particles increase the degree of graphitization for the Co–N–C catalyst during heat treatment. All these results further indicate that the preheating of ZIF-8 at 700 °C is essential to avoid Co agglomeration and generate atomic Co–Nx sites.

XPS analyses were conducted to evaluate the prepared catalysts' surface chemical composition and elemental bonding configuration. The N and Co contents in SA Co–Nx–HCM are 4.41 and 0.22 at%, respectively, similar to those in the SA Co–Nx–C catalyst (4.34 at% and 0.24 at%, Table S2†). The N 1s fitting results indicate the coexistence of pyridinic N (398.5 eV), Co–Nx (399.3 eV), pyrrolic N (400.3 eV), graphitic N (401.2 eV), and oxidized N (402.5 eV), respectively (Fig. 3e and f, S4†). Furthermore, the Co–Nx contents in the stepwise pyrolyzed samples (SA Co–Nx–HCM, 0.78 at%; SA Co–Nx–C, 0.73 at%) are higher compared to that in the direct–carbonized sample (Co–N–C, 0.63 at%, Table S3†). The Co 2p spectrum for SA Co–Nx–HCM exhibit two prominent peaks at 780.3 and 795.7 eV corresponding to the Co^{2+}–N coordinates with their satellite peaks centred at 785.2 eV (Fig. 3g). Then, X-ray absorption near-edge structure (XANES) and extended X-ray absorption fine structure (EXAFS) analyses were performed to further analyze the chemical environments of Co–Nx moieties in the catalysts. The Co K-edge spectra in Fig. 3h suggest that the features of SA Co–Nx–HCM are more similar to CoPC but different from Co foil and CoO, which further indicates the valence state of SA Co–Nx–HCM is situated between that of Co^0 and Co^{II}.[28] Further, Fourier-transformed k2-weighted EXAFS (Fig. 3i) show that the SA Co–Nx–HCM exhibits one apparent peak at ca. 1.5 Å, which was ascribed to the Co–N first coordination shell, and there is almost no Co–Co peak at 2.2 Å identified. These results suggest that the Co atoms are atomically dispersed in the Co–Nx–HCM catalyst. Moreover, this strategy is able to generate a relatively high SA Co content (1.13 wt%) compared to previously reported catalysts (Table S4†), which is beneficial for boosting the ORR.

Considering the unique assembled-spheres with a hierarchical-porous structure and the highly dense active SA Co–Nx sites, the explored SA Co–Nx–HCM catalyst could be a good candidate for catalyzing the ORR in natural electrolytes. A commercial Pt/C catalyst, Co–N–C, and SA Co–Nx–C were evaluated for comparison. The SA Co–Nx–HCM samples prepared at 900 °C exhibit the highest half-wave potential (Fig. S5†). As shown in Fig. 4a, no obvious reduction peaks were observed in the N_2-saturated PBS electrolyte, while characteristic cathode peaks appeared in the O_2-saturated electrolyte, indicating the ORR electrocatalytic activity of the prepared Co-based samples. Further, SA Co–Nx–C exhibits a more positive half-wave potential ($E_{1/2}$) of 0.69 V than Co–N–C ($E_{1/2}$ = 0.67 V), suggesting the stepwise pyrolysis could significantly improve the ORR activity (Fig. 4b). The prior spray-assisted treatment could further enhance the catalytic performance for SA Co–Nx–HCM with the best $E_{1/2}$ up to 0.71 V compared to the other catalysts. Meanwhile, SA Co–Nx–HCM also shows the largest
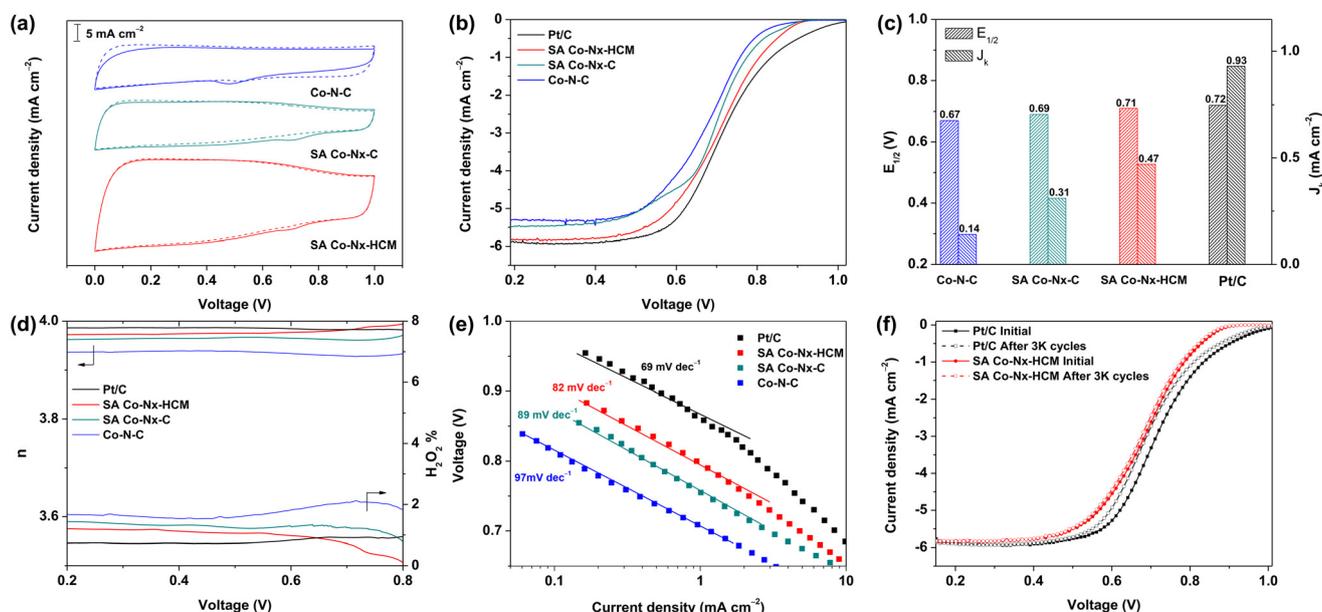

Fig. 4 (a) CV curves of the prepared catalysts in O_2- and N_2-saturated PBS electrolytes. (b) ORR polarization plots, (c) J_k at 0.85 V and $E_{1/2}$, (d) electron transfer number and H_2O_2 yield and (e) Tafel plots of the prepared catalysts. (f) ORR polarization curves of SA Co–Nx-HCM and Pt/C catalysts before and after 3000 cycles.

diffusion-limiting current density (5.81 mA cm^{-2}) compared with SA Co–Nx–C (5.41 mA cm^{-2}) and Co–N–C (5.30 mA cm^{-2}), indicating the smoothly accessible and high utilization of Co–Nx active sites. Further, the $E_{1/2}$ of SA Co–Nx–HCM is only *ca.*10 mV less than that of Pt/C ($E_{1/2} = 0.72$ V), and the limiting current density is approaching the Pt/C catalyst (5.92 mA cm^{-2}). At 0.85 V, the kinetic current density of the ORR on SA Co–Nx–HCM is 0.47 mA cm^{-2}, which is much higher than that of Co–N–C (0.14 mA cm^{-2}) and SA Co–Nx–C (0.31 mA cm^{-2}), and lower than that of Pt/C (0.93 mA cm^{-2}) (Fig. 4c). In addition, a rotating ring disk electrode (RRDE) study was conducted to evaluate the selectivity of these Co-based catalysts in a neutral electrolyte. The electron transfer number of the SA Co–Nx–HCM catalyst is above 3.97 (Fig. 4d), which is superior to those of the SA Co–Nx–C (3.95) and Co–N–C (3.93) catalysts and approaching that of the Pt/C catalyst (3.98), suggesting a high selectivity toward a four electron reaction. Also, the SA Co–Nx–HCM catalyst shows a H$_2$O$_2$ yield below 1.2% at the potential range from 0.4 to 0.9 V, which is superior to the SA Co–Nx–C (1.4%) and Co–N–C (2.0%) catalysts, suggesting the good selectivity of the oxygen reduction toward H$_2$O (Fig. 4d). The decent ORR activity of SA Co–Nx–HCM was further confirmed by its smaller Tafel slope (82 mV dec^{-1}) compared to SA Co–Nx–C (89 mV dec^{-1}) and Co–N–C (97 mV dec^{-1}), demonstrating that the SA Co–Nx–HCM electrocatalyst manifested improved ORR kinetics (Fig. 4e). Then, the electrochemical durability was evaluated to assess the catalyst's practical application. The SA Co–Nx–HCM and Pt/C benchmark were assessed and compared after 3000 CV cycles between 0.6 and 1.0 V under O$_2$ atmosphere. It shows that the

$E_{1/2}$ difference is 26 mV for Pt/C after the accelerated degradation test, while there is almost no $E_{1/2}$ change for the SA Co–Nx–HCM catalyst, unambiguously demonstrating its superior durability (Fig. 4f).

To verify the application potential of the SA Co–Nx–HCM catalyst, homemade aqueous Mg–air batteries were assembled utilizing SA Co–Nx–HCM coated carbon paper as the air-cathode in a neutral PBS electrolyte (Fig. 5a). Fig. 5b shows the surface structures of air electrodes built with SA Co–Nx–HCM and SA Co–Nx–C. It is noticeable that the microspheres make the SA Co–Nx–HCM air cathode possess ample macro-sized pores and form a 3D open porous framework, which could facilitate the rapid diffusion of air to all accessible Co-Nx active sites and thus enhance the Mg–air battery performances. As for the SA Co–Nx–C cathode, the isolated ZIF-8-derived carbon particles form a dense and blocked catalyst layer with negligible large pores, leading to a decreased mass transport capability. As depicted in Fig. 5c, the open-circuit potential of the Mg–air battery equipped with SA Co–Nx–HCM is as large as *ca.* 1.78 V, approaching that of the Pt/C catalyst of 1.81 V. The maximum power density of SA Co–Nx–HCM is up to 34.2 mW cm^{-2}, which is higher than that of SA Co–Nx–C (29.5 mW cm^{-2}), Co–N–C (23.5 mW cm^{-2}) and is approaching that of Pt/C (35.9 mW cm^{-2}). The enhanced battery performance could be ascribed to the facilitated mass transfer abilities of the SA Co–Nx–HCM cathode, which was supported by electrochemical impedance spectra in Fig. 5d. The Nyquist plots indicate that the SA Co–Nx–HCM (0.67 Ω) cathode exhibits a much lower
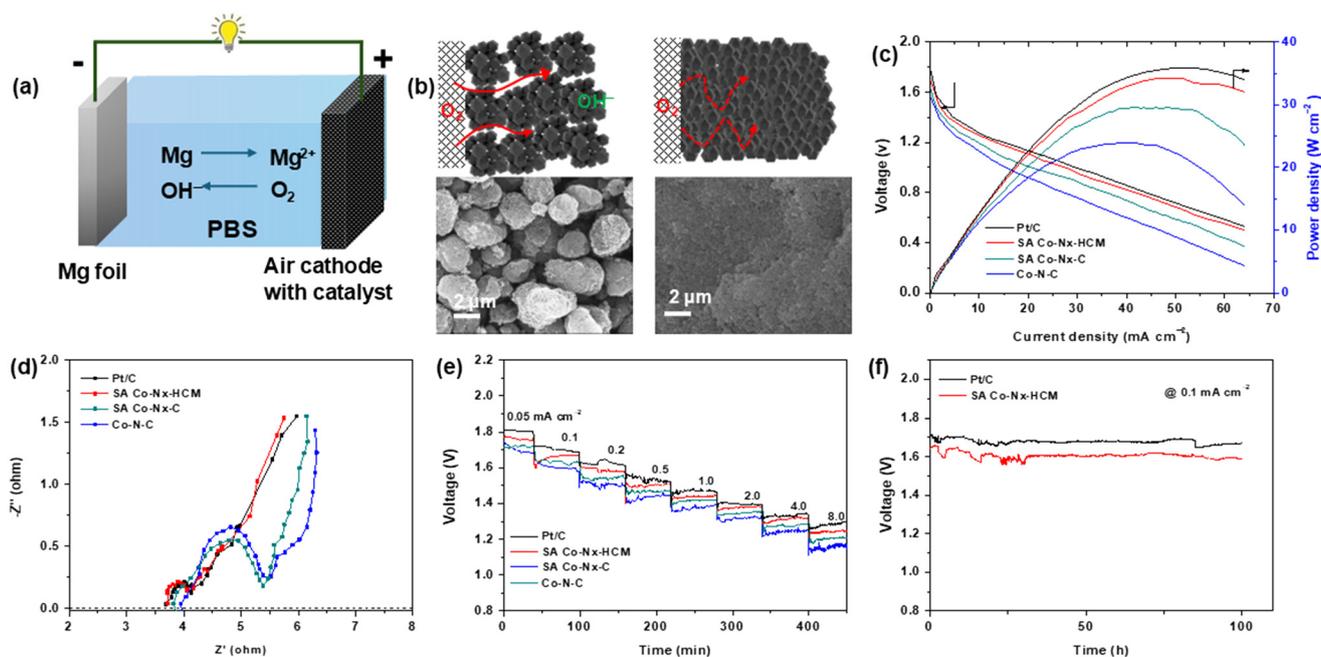

Fig. 5 (a) Schematic illustration of the liquid Mg–air battery. (b) Schematic illustrations of the air electrode and their SEM images. (c) Polarization and power density curves of Mg–air batteries with the prepared catalysts and Pt/C. (d) Nyquist plots for batteries at 0.60 V. (e) The rate discharge performance of batteries at various current densities. (f) Discharge capacity of the Mg–air batteries with SA Co–Nx–HCM and Pt/C cathodes at a current density of 0.1 mA cm^{-2} in PBS.

© 2025 The Author(s). Published by the Royal Society of Chemistry

RSC Appl. Interfaces, 2025, **2**, 696–703 | **701**

charge/mass transfer resistance than SA Co–Nx–C (1.52 Ω) and Co–N–C (1.55 Ω), suggesting that the 3D open porous electrode could sharply enhance mass transfer efficiency and thus construct robust triple phase interfaces for the ORR. Then the discharge performances for air electrodes at different current densities were evaluated. (Fig. 5f). Notably, SA Co–Nx–HCM shows a small voltage drop at the current density range of 0.05–8.0 mA cm^{-2}. The SA Co–Nx–HCM air cathode delivers voltage plateaus of 1.76 and 1.24 V at the discharge current densities of 0.05 and 8 mA cm^{-2}, which are superior to the SA Co–Nx–C (1.72 and 1.20 V) and Co–N–C (1.68 and 1.16 V) catalyst assembled batteries. Meanwhile, the SA Co–Nx–HCM based battery delivers an energy density of 3441 Wh kg$_{Mg}^{-1}$ at 0.1 mA cm^{-2}, which is close to the Pt/C based battery (3573 Wh kg$_{Mg}^{-1}$) (Fig. S6†). In addition, the SA Co–Nx–HCM electrocatalyst works stably in a primary Mg-air battery at a current density of 0.1 mA cm^{-2}. After 100 h of operation, the discharge voltage remains nearly unchanged, indicating the superior stability of SA Co–Nx–HCM in the Mg–air battery. (Fig. 5f).

Conclusion

In summary, hierarchical carbon microspheres coupled with single atomic Co–Nx active sites were generated simultaneously by a spray-assisted stepwise pyrolysis strategy. The dense Co–Nx moieties endow the SA Co–Nx–HCM catalyst with good cytocompatibility, excellent ORR activity, and stability. In addition, the hierarchical carbon microspheres also manifested high mass transfer efficiency in the air cathode and boosted reaction kinetics. Moreover, using the SA Co–Nx–HCM catalyst assembly, a Mg–air battery delivers superior discharge ability and durability. This work provides a new way for rationally designing highly active electrocatalysts for the ORR and other energy-conversion-related catalytic reactions.

Data availability

The data supporting this article have been included as part of the ESI.†

Conflicts of interest

The authors declare no conflict of interest.

Acknowledgements

References

1 E. J. Bradbury, L. D. F. Moon, R. J. Popat, V. R. King, G. S. Bennett, P. N. Patel, J. W. Fawcett and S. B. McMahon, *Nature*, 2002, **416**, 636–640.

2 T. Zhang, Z. Tao and J. Chen, *Mater. Horiz.*, 2014, **1**, 196–206.

3 D. Yan, D. Tao, D. Xu, Y. Sun, B. Deng, G. Cao, J. Fang and W. Xu, *Nano Energy*, 2024, **129**, 110000.

4 G. Song, *Corros. Sci.*, 2007, **49**, 1696–1701.

5 C. Yu, C. Wang, X. Liu, X. Jia, S. Naficy, K. Shu, M. Forsyth and G. G. Wallace, *Adv. Mater.*, 2016, **28**, 9349–9355.

6 J. Zhang, H. Zhang, Y. Zhang, X. Wang, H. Li, F. Feng, K. Wang, G. Zhang, S. Sun and Y. Zhang, *J. Mater. Chem. A*, 2023, **11**, 7924–7948.

7 Z. Xi, J. Han, Z. Jin, K. Hu, H.-J. Qiu and Y. Ito, *Small*, 2024, **20**, 2308045.

8 M. P. Staiger, A. M. Pietak, J. Huadmai and G. Dias, *Biomaterials*, 2006, **27**, 1728–1734.

9 Y. Yamasaki, Y. Yoshida, M. Okazaki, A. Shimazu, T. Kubo, Y. Akagawa and T. Uchida, *Biomaterials*, 2003, **24**, 4913–4920.

10 X. Chen, X. Liu, Q. Le, M. Zhang, M. Liu and A. Atrens, *J. Mater. Chem. A*, 2021, **9**, 12367–12399.

11 J.-S. Lee, S. Tai Kim, R. Cao, N.-S. Choi, M. Liu, K. T. Lee and J. Cho, *Adv. Energy Mater.*, 2011, **1**, 34–50.

12 C.-S. Li, Y. Sun, F. Gebert and S.-L. Chou, *Adv. Energy Mater.*, 2017, **7**, 1700869.

13 Y. Sun, X. Liu, Y. Jiang, J. Li, J. Ding, W. Hu and C. Zhong, *J. Mater. Chem. A*, 2019, **7**, 18183–18208.

14 Y. Dou, S. Xing, Z. Zhang and Z. Zhou, *Electrochem. Energy Rev.*, 2024, **7**, 6.

15 J. Li, S. Chen, N. Yang, M. Deng, S. Ibraheem, J. Deng, J. Li, L. Li and Z. Wei, *Angew. Chem., Int. Ed.*, 2019, **58**, 7035–7039.

16 Y. He, S. Liu, C. Priest, Q. Shi and G. Wu, *Chem. Soc. Rev.*, 2020, **49**, 3484–3524.

17 X. Fu, G. Jiang, G. Wen, R. Gao, S. Li, M. Li, J. Zhu, Y. Zheng, Z. Li, Y. Hu, L. Yang, Z. Bai, A. Yu and Z. Chen, *Appl. Catal., B*, 2021, **293**, 120176.

18 X. Li, X. Huang, S. Xi, S. Miao, J. Ding, W. Cai, S. Liu, X. Yang, H. Yang, J. Gao, J. Wang, Y. Huang, T. Zhang and B. Liu, *J. Am. Chem. Soc.*, 2018, **140**, 12469–12475.

19 J. Hu, W. Liu, C. Xin, J. Guo, X. Cheng, J. Wei, C. Hao, G. Zhang and Y. Shi, *J. Mater. Chem. A*, 2021, **9**, 24803–24829.

20 M. Wu, F. Dong, Y. Yang, X. Cui, X. Liu, Y. Zhu, D. Li, S. Omanovic, S. Sun and G. Zhang, *Electrochem. Energy Rev.*, 2024, **7**, 10.

21 W.-X. Hong, W.-H. Wang, Y.-H. Chang, H. Pourzolfaghar, I. H. Tseng and Y.-Y. Li, *Nano Energy*, 2024, **121**, 109236.

22 L. Jiao, G. Wan, R. Zhang, H. Zhou, S.-H. Yu and H.-L. Jiang, *Angew. Chem., Int. Ed.*, 2018, **57**, 8525–8529.

23 H. Zhang, H. T. Chung, D. A. Cullen, S. Wagner, U. I. Kramm, K. L. More, P. Zelenay and G. Wu, *Energy Environ. Sci.*, 2019, **12**, 2548–2558.

24 S. Shen, Y. Sun, H. Sun, Y. Pang, S. Xia, T. Chen, S. Zheng and T. Yuan, *Catalysts*, 2022, **12**, 525.

25 Q. Zhang, P. Liu, X. Fu, Y. Yuan, L. Wang, R. Gao, L. Zheng, L. Yang and Z. Bai, *Adv. Funct. Mater.*, 2022, **32**, 2112805.

702 | *RSC Appl. Interfaces*, 2025, **2**, 696–703

© 2025 The Author(s). Published by the Royal Society of Chemistry

26 P. Yin, T. Yao, Y. Wu, L. Zheng, Y. Lin, W. Liu, H. Ju, J. Zhu, X. Hong, Z. Deng, G. Zhou, S. Wei and Y. Li, *Angew. Chem., Int. Ed.*, 2016, **55**, 10800–10805.

27 Z. Wang, H. Jin, T. Meng, K. Liao, W. Meng, J. Yang, D. He, Y. Xiong and S. Mu, *Adv. Funct. Mater.*, 2018, **28**, 1802596.

28 Z. Lu, B. Wang, Y. Hu, W. Liu, Y. Zhao, R. Yang, Z. Li, J. Luo, B. Chi, Z. Jiang, M. Li, S. Mu, S. Liao, J. Zhang and X. Sun, *Angew. Chem., Int. Ed.*, 2019, **58**, 2622–2626.

29 L. Zhang, J. M. T. A. Fischer, Y. Jia, X. Yan, W. Xu, X. Wang, J. Chen, D. Yang, H. Liu, L. Zhuang, M. Hankel, D. J. Searles, K. Huang, S. Feng, C. L. Brown and X. Yao, *J. Am. Chem. Soc.*, 2018, **140**, 10757–10763.

30 D. Yu, Y. Ma, F. Hu, C.-C. Lin, L. Li, H.-Y. Chen, X. Han and S. Peng, *Adv. Energy Mater.*, 2021, **11**, 2101242.

31 C. P. K. Prabhu, K. R. Naveen and J. Hur, *RSC Appl. Interfaces*, 2024, **1**, 301–312.

32 Y. Zhou, R. Lu, X. Tao, Z. Qiu, G. Chen, J. Yang, Y. Zhao, X. Feng and K. Müllen, *J. Am. Chem. Soc.*, 2023, **145**, 3647–3655.

33 P. Yao, J. Cao, X. Gong, C. Han, M. Ruan, P. Song and W. Xu, *J. Phys. Chem. C*, 2021, **125**, 9839–9846.

34 S. Son, D. Lim, D. Nam, J. Kim, S. E. Shim and S.-H. Baeck, *J. Solid State Chem.*, 2019, **274**, 237–242.

35 C. Gao, S. Mu, R. Yan, F. Chen, T. Ma, S. Cao, S. Li, L. Ma, Y. Wang and C. Cheng, *Small*, 2022, **18**, 2105409.

36 M. Liu, Q. Xu, Q. Miao, S. Yang, P. Wu, G. Liu, J. He, C. Yu and G. Zeng, *J. Mater. Chem. A*, 2022, **10**, 228–233.

37 L. Zheng, Y. Zhao, H. Zhang, W. Xia and J. Tang, *ChemSusChem*, 2022, **15**, e202102642.

38 Y. J. Sa, D.-J. Seo, J. Woo, J. T. Lim, J. Y. Cheon, S. Y. Yang, J. M. Lee, D. Kang, T. J. Shin, H. S. Shin, H. Y. Jeong, C. S. Kim, M. G. Kim, T.-Y. Kim and S. H. Joo, *J. Am. Chem. Soc.*, 2016, **138**, 15046–15056.

39 X. Fu, N. Li, B. Ren, G. Jiang, Y. Liu, F. M. Hassan, D. Su, J. Zhu, L. Yang, Z. Bai, Z. P. Cano, A. Yu and Z. Chen, *Adv. Energy Mater.*, 2019, **9**, 1803737.

40 Y. He, Q. Shi, W. Shan, X. Li, A. J. Kropf, E. C. Wegener, J. Wright, S. Karakalos, D. Su, D. A. Cullen, G. Wang, D. J. Myers and G. Wu, *Angew. Chem., Int. Ed.*, 2021, **60**, 9516–9526.

41 S. Li, C. Cheng, X. Zhao, J. Schmidt and A. Thomas, *Angew. Chem., Int. Ed.*, 2018, **57**, 1856–1862.

42 X. Fu, P. Zamani, J.-Y. Choi, F. M. Hassan, G. Jiang, D. C. Higgins, Y. Zhang, M. A. Hoque and Z. Chen, *Adv. Mater.*, 2017, **29**, 1604456.

43 Y. Han, Y.-G. Wang, W. Chen, R. Xu, L. Zheng, J. Zhang, J. Luo, R.-A. Shen, Y. Zhu, W.-C. Cheong, C. Chen, Q. Peng, D. Wang and Y. Li, *J. Am. Chem. Soc.*, 2017, **139**, 17269–17272.

44 G. Chen, P. Liu, Z. Liao, F. Sun, Y. He, H. Zhong, T. Zhang, E. Zschech, M. Chen, G. Wu, J. Zhang and X. Feng, *Adv. Mater.*, 2020, **32**, 1907399.

45 J. Yu, B.-Q. Li, C.-X. Zhao, J.-N. Liu and Q. Zhang, *Adv. Mater.*, 2020, **32**, 1908488.

46 X. Wan, X. Liu, Y. Li, R. Yu, L. Zheng, W. Yan, H. Wang, M. Xu and J. Shui, *Nat. Catal.*, 2019, **2**, 259–268.

47 A. H. A. Monteverde Videla, L. Osmieri, M. Armandi and S. Specchia, *Electrochim. Acta*, 2015, **177**, 43–50.

48 X. Yang, Y. Wang, G. Zhang, L. Du, L. Yang, M. Markiewicz, J.-y. Choi, R. Chenitz and S. Sun, *Appl. Catal., B*, 2020, **264**, 118523.

49 X. Fu, R. Gao, G. Jiang, M. Li, S. Li, D. Luo, Y. Hu, Q. Yuan, W. Huang, N. Zhu, L. Yang, Z. Mao, J. Xiong, A. Yu, Z. Chen and Z. Bai, *Nano Energy*, 2021, **83**, 105734.

50 X. Zhang, Y. Li, D. He, Z. Ma, K. Liu, K. Xue and H. Li, *Chem. Eng. J.*, 2021, **425**, 130677.

51 J. Li, L. Jiao, E. Wegener, L. L. Richard, E. Liu, A. Zitolo, M. T. Sougrati, S. Mukerjee, Z. Zhao, Y. Huang, F. Yang, S. Zhong, H. Xu, A. J. Kropf, F. Jaouen, D. J. Myers and Q. Jia, *J. Am. Chem. Soc.*, 2020, **142**, 1417–1423.

52 F. Jaouen, M. Lefèvre, J.-P. Dodelet and M. Cai, *J. Phys. Chem. B*, 2006, **110**, 5553–5558.

53 J. Li, H. Zhang, W. Samarakoon, W. Shan, D. A. Cullen, S. Karakalos, M. Chen, D. Gu, K. L. More, G. Wang, Z. Feng, Z. Wang and G. Wu, *Angew. Chem., Int. Ed.*, 2019, **58**, 18971–18980.

54 H. Zhang, S. Hwang, M. Wang, Z. Feng, S. Karakalos, L. Luo, Z. Qiao, X. Xie, C. Wang, D. Su, Y. Shao and G. Wu, *J. Am. Chem. Soc.*, 2017, **139**, 14143–14149.

55 S. Gupta, S. Zhao, O. Ogoke, Y. Lin, H. Xu and G. Wu, *ChemSusChem*, 2017, **10**, 774–785.

© 2025 The Author(s). Published by the Royal Society of Chemistry

RSC Appl. Interfaces, 2025, **2**, 696–703 | **703**